ber) to the measured shear spectrum equaled 1/3. This threshold was selected heuristically, and the resulting ε and K_ρ are insensitive to the exact choice of value. $\langle V_{z\text{-}GM}^2 \rangle$ was computed by integrating the GM N-normalized shear spectrum within the same wavelengths as for $\langle V_z^2 \rangle$. To estimate $F(R_\omega)$, a bulk shear-to-strain ratio (37) was diagnosed as $R_\omega = \langle V_z^2 \rangle / (N^2 \langle \xi_z^2 \rangle)$. Here, $\langle \xi_z^2 \rangle$ is the variance of strain, the vertical gradient in the vertical displacement of isopycnals induced by internal waves. We estimated strain from CTD density profiles using a scale separation assumption (20) and calculated $\langle \xi_z^2 \rangle$ (and R_ω) in 320-m segments identical to $\langle V_z^2 \rangle$ bins. Despite being somewhat noisy, the resulting R_ω distribution shows a consistent mean value of 8 to 12 between different regions and cruises. We thus used a constant $F(R_\omega)$ of 1/3 throughout the analysis. That value is a conservative choice based on an internal wave dynamical model (39) validated with microstructure observations (37).

17. Our in situ estimates of widespread large K_ρ values show some resemblance to diapycnal diffusivities diagnosed by an inverse calculation using ACC hydrographic observations (40).

18. The vertically integrated dissipation rate E is calculated as $\int \rho \varepsilon dz$, where ρ is the in situ density, and the integral spans the entire water column.

19. This factor is assumed to include temporal variability, as suggested by the analysis of three repeats of the eastern Drake Passage transect (Fig. 1, station C) yielding very similar diffusivities.

20. C. Mauritzen, K. L. Polzin, M. S. McCartney, R. C. Millard, D. E. West-Mack, J. Geophys. Res. 107, 3147 (2002).

21. A. C. Naveira Garabato, K. L. Polzin, B. A. King, K. J. Heywood, M. Visbeck, data not shown.

22. T. D. Finnigan, D. S. Luther, R. Lukas, J. Phys. Oceanogr. 32, 2988 (2002).

23. Our ability to detect turbulent overturns in density profiles is limited by the vertical and density resolutions of the CTD system. A spectral analysis of the vertical variability of N^2 reveals that the vertical resolution is ~15 m, a consequence of the heaving of the package in the large Southern Ocean swell. The density resolution was determined as 10^{-3} kg m^{-3} from inspection of low-N data segments. Given that the vertical resolution is often the limiting factor in our data set, an estimate of how energetic the turbulence needs to be for turbulent overturns to be resolved can be made. Using a scaling argument (22), the root mean square overturn scale (the Thorpe scale, L_T) can be related to a dissipation scale [the Ozmidov scale, $L_O = (\varepsilon/N^3)^{1/2}$] by a constant of proportionality close to unity; that is, $L_T \sim L_O$. Empirically, L_T has been shown to be a factor of $\pi - 2\pi$ smaller than the vertical scales of overturns, so we expect to resolve L_T values of ~5 m. Thus, from (13) and the expression for L_O, the minimum diapycnal diffusivity resolved by an overturn analysis will be $K_\rho = R_f/(1 - R_f) \times (\varepsilon/N^2) \sim R_f/(1 - R_f) \times (L_T^2 N) \sim 10^{-3}$ m^2 s^{-1}, where a value of $N \sim 7 \times 10^{-4}$ s^{-1} typical of the deep Southern Ocean has been used.

24. Our results suggest that the diapycnal mixing required to close the abyssal heat budget of the Scotia Sea (25) occurs in two distinct regimes. In the interior of the basin, K_ρ at the neutral density surface (28.31 kg m^{-3}) used in the abyssal heat budget is in the range $K_\rho^{int} \approx 2 \times 10^{-4}$ m^2 s^{-1} to 2×10^{-3} m^2 s^{-1}, whereas it is one to two orders of magnitude larger ($K_\rho^{dbc} \approx 5 \times 10^{-3}$ m^2 s^{-1} to 5×10^{-1} m^2 s^{-1}) in the deep boundary current conveying Antarctic Bottom Water into the basin and along its southern boundary (Fig. 1). Taking intermediate values of K_ρ^{int} and K_ρ^{dbc} and assuming that our sampling locations are representative, K_ρ^{dbc} should apply over around one-tenth of the control area to produce a basin-average K_ρ^{av} of $3.9 \pm 1 \times 10^{-3}$ m^2 s^{-1}. The resulting area (~7 $\times$ 10^4 km^2) broadly corresponds with that of the deep boundary current in our hydrographic observations north of the South Scotia Ridge (Fig. 1), although the uncertainty in this scaling argument is large (greater than a factor of 3).

25. K. J. Heywood, A. C. Naveira Garabato, D. P. Stevens, Nature 415, 1011 (2002).

26. C. S. Law, E. R. Abraham, A. J. Watson, M. I. Liddicoat, J. Geophys. Res. 108, 3272 (2003).

27. K. L. Polzin, J. Phys. Oceanogr., in press.

28. K. L. Polzin, in Internal Wave Modelling: Proceedings, 'Aha Huliko'a Hawaiian Winter Workshop, P. Müller, D. Henderson, Eds. (special publication of the School of Ocean and Earth Science and Technology, Univ. of Hawaii, Honolulu, HI, 1999), pp. 117–128.

29. C. Wunsch, J. Phys. Oceanogr. 28, 2332 (1998).

30. K. D. Leaman, T. B. Sanford, J. Geophys. Res. 15, 1975 (1975).

31. M. H. Alford, Geophys. Res. Lett. 30, 1424 (2003).

32. An application of an earlier version of our technique to 12 LADCP velocity profiles downstream of the Kerguelen Plateau (41) indeed revealed enhanced ($K_\rho \geq 10^{-4}$ m^2 s^{-1}) diapycnal mixing in the region below a depth of 500 to 1000 m.

33. K. Speer, S. R. Rintoul, B. M. Sloyan, J. Phys. Oceanogr. 30, 3212 (2000).

34. This is exemplified by the high sensitivity of the Southern Ocean MOC in a zonal channel model to the prescribed diapycnal buoyancy flux divergence (42).

35. Near-local dissipation of the ~8 $\times$ 10^{11} W input by the wind into the Southern Ocean general circulation would imply an ACC-mean vertically integrated dissipation rate $E \sim 10^{-2}$ W m^{-2} (29). If representative of other regions, our inference of $E \sim 1 \times 10^{-2}$ W m^{-2} to 3×10^{-2} W m^{-2} in the Scotia Sea and near the Kerguelen Plateau (28), combined with background values an order of magnitude smaller, indicates that diapycnal mixing hot spots would need to occupy a substantial fraction (roughly one-third) of the ACC region to dissipate the bulk of the wind work. The abundance of complex topography along the current's path suggests that an energy budget closure of this type may apply.

36. T. R. Osborn, J. Phys. Oceanogr. 20, 83 (1980).

37. K. L. Polzin, J. M. Toole, R. W. Schmitt, J. Phys. Oceanogr. 25, 306 (1995).

38. C. J. R. Garrett, W. H. Munk, J. Geophys. Res. 80, 291 (1975).

39. E. S. Henyey, J. Wright, S. M. Flatté, J. Geophys. Res. 91, 8487 (1986).

40. D. Olbers, M. Wenzel, in Oceanic Circulation Models: Combining Data and Dynamics, D. L. T. Anderson, J. Willebrand, Eds. (Kluwer Academic, Dordrecht, Netherlands, 1989), pp. 95–139.

41. K. L. Polzin, E. Firing, Int. WOCE Newsl. 29, 39 (1997).

42. R. H. Karsten, H. Jones, J. Marshall, J. Phys. Oceanogr. 32, 39 (2003).

43. W. H. F. Smith, D. T. Sandwell, Science, 277, 1956 (1997).

44. A. H. Orsi, T. Whitworth, W. D. Nowlin, Deep-Sea Res. I 42, 641 (1995).

45. A Natural Environment Research Council postdoctoral research fellowship supported A.C.N.G. during the analysis and writing of this report. Feedback from L. Goldson, E. Kunze, R. Muench, B. Oliver, B. Sloyan, K. Speer, K. Stansfield, A. Watson, and two anonymous reviewers is gratefully acknowledged.

Virus-Based Toolkit for the Directed Synthesis of Magnetic and Semiconducting Nanowires

Chuanbin Mao,[1]* Daniel J. Solis,[4]* Brian D. Reiss,[5] Stephen T. Kottmann,[4] Rozamond Y. Sweeney,[2] Andrew Hayhurst,[2] George Georgiou,[2,3] Brent Iverson,[1,2] Angela M. Belcher[5]†

We report a virus-based scaffold for the synthesis of single-crystal ZnS, CdS, and freestanding chemically ordered CoPt and FePt nanowires, with the means of modifying substrate specificity through standard biological methods. Peptides (selected through an evolutionary screening process) that exhibit control of composition, size, and phase during nanoparticle nucleation have been expressed on the highly ordered filamentous capsid of the M13 bacteriophage. The incorporation of specific, nucleating peptides into the generic scaffold of the M13 coat structure provides a viable template for the directed synthesis of semiconducting and magnetic materials. Removal of the viral template by means of annealing promoted oriented aggregation-based crystal growth, forming individual crystalline nanowires. The unique ability to interchange substrate-specific peptides into the linear self-assembled filamentous construct of the M13 virus introduces a material tunability that has not been seen in previous synthetic routes. Therefore, this system provides a genetic toolkit for growing and organizing nanowires from semiconducting and magnetic materials.

The reliance of future technologies on developing scalable and economic methods for the fabrication of one-dimensional (1D) systems has spurred intense and rapid progress in the area of materials synthesis. In particular, 1D materials have been enthusiastically pursued for their applications in the study of electrical transport (1), optical phenomena (2), and as functional units in nanocircuitry (3). Pursuit of "bottom-up" methods for the synthesis of semiconducting, metallic, and magnetic nanowires has yielded strategies including, but not limited to, vapor liquid solid (VLS) (4), chemical (5), solvothermal, vapor phase, and template-directed fabrication (6). Although each method developed for the production of nanowires has had success in achieving high-quality materials, no distinct strategy to date has yielded monodisperse, crystalline nanowires of radically different compositions. The realization of such a system

[1]Departments of Chemistry and Biochemistry, [2]Institute for Cellular and Molecular Biology, [3]Department of Chemical Engineering, University of Texas (UT) at Austin, Austin, TX 78712, USA. [4]Department of Chemistry, [5]Department of Materials Science and Engineering and Biological Engineering Division, Massachusetts Institute of Technology (MIT), Cambridge, MA 02139–4307, USA.

*These authors contributed equally to this work.
†To whom correspondence should be addressed. E-mail: belcher@mit.edu

would require the combination of substrate-specific ligands with the predictability of self-assembly that is commonly found in nature. Recently, biological factors have been exploited as synthesis directors for nanofibers (*7*, *8*), virus-based particle cages (*9*), virus-particle assemblies (*10*, *11*), and nonspecific peptide templates (*12*). This is due to the high degree of organization, ease of chemical modification, and naturally occurring self-assembly motifs inherent in these systems.

The ability to store information about a material, including composition, phase, and crystallographic detail, within the genetic code of the M13 bacteriophage virus DNA has proven to be a viable means of synthesizing and organizing materials on the nanometer scale. The use of phage display techniques (using peptide libraries consisting of $\sim 10^9$ random sequences) has led to the discovery of materials-specific peptides that have preferential binding (*13*), control over nanoparticle nucleation (*14*), and the ability to order on the basis of the inherent shape anisotropy of the filamentous M13 virus (*11*). Because the protein sequences responsible for these attributes are gene linked and contained within the capsid of

the virus, exact genetic copies of the virus scaffold are easily reproduced by infection into its bacterial host.

We report the general synthesis of 1D nanostructures based on a genetically modified virus scaffold for the directed growth and assembly of crystalline nanoparticles into 1D arrays, followed by annealing of the virus-particle assemblies into high aspect ratio crystalline nanowires through oriented aggregation-based crystal growth (*15*, *16*) (Fig. 1A). The synthesis of analogous nanowire structures from fundamentally different materials, the II-VI semiconductors ZnS and CdS and the crystal structure $L1_0$ ferromagnetic alloys CoPt and FePt, demonstrates both the generality of the virus scaffold and the ability to precisely control material characteristics through genetic modification. In contrast to other synthetic methods (*6*), this approach allows for the genetic control of crystalline semiconducting, metallic, oxide, and magnetic materials with a universal template.

Evolution of substrate-specific peptides through phage display technologies for the directed nucleation of materials on the nanometer scale has been previously reported and serves as the basis for the ma-

terial specificity in the virus template (*13*). Screening of the ZnS, CdS (*14*, *17*), FePt, and CoPt systems (*18*) with commercially available bacteriophage libraries (New England Biolabs) expressing either a disulphide constrained (Cys-Cys) heptapeptide or a linear dodecapeptide as a fusion to the gene product (gP) 3 protein located at the proximal tip of the virus has yielded nucleating peptides with the following sequences: CNNPMHQNC (termed A7; ZnS), SLTPLTTSHLRS (termed J140; CdS), HNKHLPSTQPLA (termed FP12; FePt), and CNAGDHANC (termed CP7; CoPt) (*19*). The incorporation of these peptides into the highly ordered, self-assembled capsid of the M13 bacteriophage virus provides a linear template that can simultaneously control particle phase and composition, while maintaining an ease of material adaptability through genetic tuning of the basic protein building blocks.

The M13 bacteriophage is a high–production rate virus (200 mg/liter) comprising five genetically modifiable proteins (*20*–*22*): gP3, gP6, gP7, gP8, and gP9. About 2700 copies of the gP8 protein form the capsid of the wild-type virus. The gP8 protein was genetically modified and expressed using a phagemid system, resulting in the fusion of the substrate-specific peptides to the N terminus of the gP8 protein (*14*). During assembly, stacking of the gP8 unit cell results in a fivefold symmetry down the length (*c* axis) of the virus; this stacking is also the origin of the ordering of fusion peptides in a 3D structure (Fig. 1B). Computational analysis of peptide expression on the capsid of the virus revealed that the nearest neighbor peptide separation stabilized around 3 nm at and above 20% incorporation (Fig. 1C). Consequently, high incorporation of the substrate-specific fusion peptides is not required for complete mineralization of the virus to occur. Trifunctional templates can be realized through further genetic modification of the proximal and remote tips of the virus [specifically, the gP3 and gP9 proteins (*23*)], which can be used to push the current system to higher aspect ratios and introduce materials that we screened, including noble metals, semiconductors, and oxides, to assemble functional heterostructured materials (Fig. 1D).

Mineralization of the ZnS and CdS systems has been described previously (*11*, *14*, *17*); the process involves incubating the viral template with metal salt precursors at reduced temperatures to promote uniform orientation of the peptide molecules during nucleation (*24*), which leads to the preferred crystallographic orientation of nucleated nanocrystals. Before annealing, wurtzite ZnS and CdS nanocrystals (3 to 5 nm) that were grown on the virus surface were in close contact and preferentially oriented with the [001] direc-
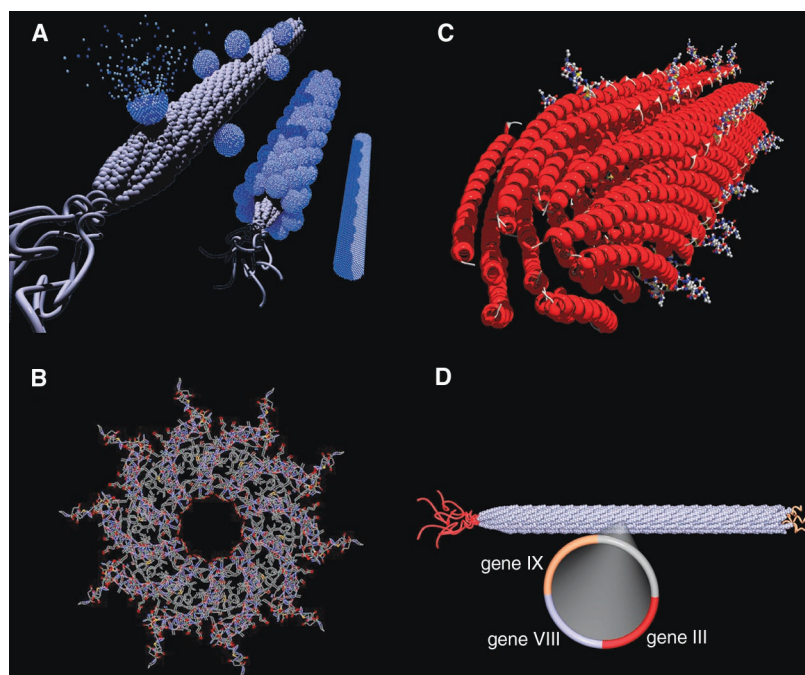

Fig. 1. Visualization of the M13 bacteriophage and the subsequent nanowire synthesis. The gP8 coat assembly was reconstructed from the x-ray fiber crystallographic data (PDB number 1ifj). The gP3 and gP9 proteins located at the proximal and remote ends of the virus are not to scale and serve as representations of the proteins. (**A**) The nanowire synthesis scheme is visualized for the nucleation, ordering, and annealing of virus-particle assemblies. (**B**) The symmetry of the virus allows for ordering of the nucleated particles along the *x*, *y*, and *z* directions, fulfilling the requirements for aggregation-based annealing. (**C**) The highly ordered nature of the self-assembled M13 bacteriophage promotes the preferred orientation seen in nucleated particles through the rigidity and packing of the expressed peptides, which is visualized at 20% incorporation. (**D**) The construct of the M13 bacteriophage virus showing the genetically modifiable capsid and ends, specifically the gP3, gP8, and gP9, which are coded for in the phagemid DNA enclosed within the virus capsid.

tion and the (100) (ZnS) and (001) (CdS) planes, which were perpendicular to the wire-length direction. These data are supported by electron diffraction (ED), high-resolution transmission electron microscopy (HRTEM), high-angle annular dark-field scanning transmission electron microscopy (HAADF-STEM), and dark-field diffraction-contrast imaging (Fig. 2) (25). Particles attached to the virus were prohibited from fusing under initial synthesis conditions because of the blocking effects of the nucleating peptides, and they therefore required removal of the template to form single-crystal nanowires. Thermal gravimetric analysis of the virus-particle system was used to obtain a critical temperature for the synthesis of crystalline nanowires, and it showed removal of the organic materials by 350°C (26). This agreed well with the minimum temperature observed for the fusion of adjacent particles by TEM with annealing, which we performed in situ using a thermal stage (27).

Annealing of the mineralized viruses at temperatures below the ZnS and CdS particle melting point (400° to 500°C) allowed the polycrystalline assemblies to form single-crystal nanowires through the removal of the organic template and the minimization of the interfacial energy (28) (Fig. 2, B and E, wires measure 600 to 650 nm in length for ZnS and 475 to 500 nm for CdS; both have diameters of ~20 nm). ED and HRTEM revealed the single-crystal nature of individual nanowires that inherited the preferred orientation seen in the precursor polycrystalline wires when the grain boundaries were removed (29, 30) (Fig. 2, C and D). The [100] direction and (001) plane orientations of the observed ZnS nanowires were consistent with common elongation directions for II-VI nanowires, even though these are thermodynamically high-energy planes (Fig. 2, B and C) (15, 16, 31). HRTEM of the single-crystal CdS nanowires revealed a lattice spacing of 2.4 Å, which was consistent with the unique 2.4519 Å separation between two (102) planes in bulk wurtzite CdS crystals [Joint Committee on Powder Diffraction Standards (JCPDS) card number 41-1049]. The 43.1° orientation of (102) lattice planes with respect to the nanowire axis indicated that the nanowire was elongated along the [001] direction and again confirmed the wurtzite structure (Fig. 2F).

Extending the virus-directed synthesis approach to the ferromagnetic $L1_0$ CoPt and FePt systems was a natural direction for both demonstrating the diversity of applicable materials and addressing current technological issues regarding the development of low-dimensional magnetic materials. Platinum-alloyed magnetic materials of the chemically ordered $L1_0$ phase have

been of recent interest because of their high coercivity, resistance to oxidation, and inherent magnetic anisotropy, which are necessary for ultrahigh-density recording media (32). Although synthetic routes such as VLS yield exquisite 1D semiconducting structures, and nonspecific template schemes are applicable to a range of mate-
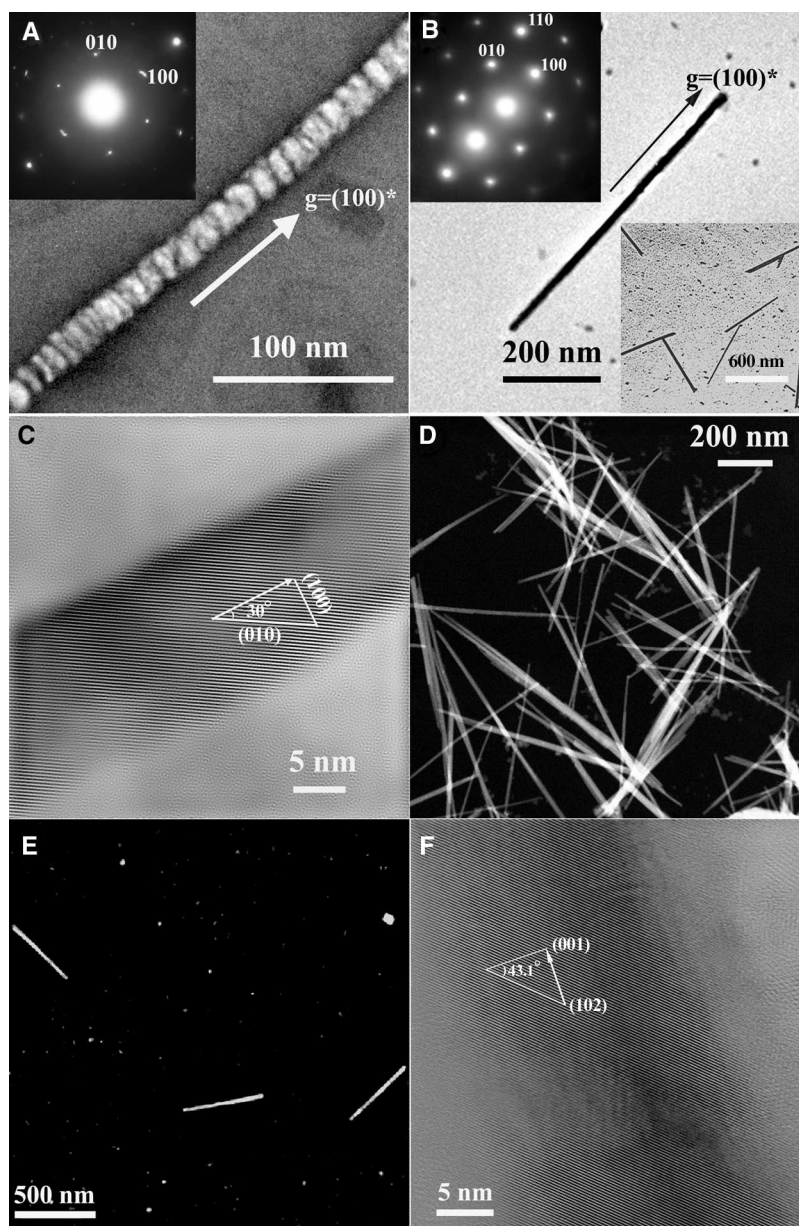

Fig. 2. Electron microscopy of both the pre- and postannealed ZnS and CdS viral nanowires. (**A**) Dark-field diffraction-contrast imaging of the pre-annealed ZnS system using the (100) reflection reveals the crystallographic ordering of the nucleated nanocrystals, in which contrast stems from satisfying the (100) Bragg diffraction condition. (Inset) ED pattern of the polycrystalline pre-annealed wire showing the wurtzite crystal structure and the single-crystal type [001] zone axis pattern, suggesting a strong [001] zone axis preferred orientation of the nanocrystals on the viral template. g = (100)* denotes the reciprocal vector of (100) crystal planes, which is perpendicular to the (100) planes and has a length inversely proportional to the interplanar spacing of the (100) planes. (**B**) Bright-field TEM image of an individual ZnS single-crystal nanowire formed after annealing. (Inset, upper left) ED pattern along the [001] zone axis shows a single-crystal wurtzite structure of the annealed ZnS nanowire. (Inset, lower right) Low-magnification TEM image showing the monodisperse, isolated single-crystal nanowires. (**C**) A typical HRTEM of a ZnS single-crystal nanowire showing a lattice image that continually extends the length of the wire, confirming the single-crystal nature of the annealed nanowire. The measured lattice spacing of 0.33 nm corresponds to the (010) planes in wurtzite ZnS crystals. A 30° orientation of (010) lattice planes with respect to the nanowire axis is consistent with the (100) growth direction determined by ED. (**D**) HAADF-STEM image of single-crystal ZnS nanowires, which were annealed on a silicon wafer. (**E**) HAADF-STEM images of CdS single-crystal nanowires. (**F**) A HRTEM lattice image of an individual CdS nanowire. The experimental lattice fringe spacing, 0.24 nm, is consistent with the unique 0.24519-nm separation between two (102) planes in bulk wurtzite CdS crystals.

rials, both have faced difficulties in producing high-quality, crystalline, metallic, and magnetic nanowires in freestanding form (*33*).

The M13 bacteriophage was modified by fusing either the CP7 CoPt-specific or FP12 FePt-specific peptide into the virus capsid. Nucleation of the CoPt and FePt particles was achieved by means of the chemical reduction of metal precursor salts in the presence of gP8-modified viruses (*18*, *34*). Annealing of the assemblies at 350°C was necessary for the removal of the virus template, and it promoted the growth of crystalline CoPt and FePt nanowires that retained the $L1_0$ phase of the as-prepared particles and that were uniform in diameter (10 nm ± 5%). The crystalline nature of the wires can be seen in the selected area ED pattern, which also shows the characteristic (001) and (110) $L1_0$ peaks, and in HRTEM lattice imaging (Fig. 3, C and D). The (111) plane that was perpendicular to the long axis of the CoPt wires and that had a lattice spacing of 2.177 Å was in agreement with the reported value of 2.176 Å, which again confirmed the highly crystalline nature of the material (Fig. 3D, JCPDS number 43-1358). The persistence of the $L1_0$ phase, which has traditionally been accessible only above 550°C (*35*), was attributed to the propensity of particles to maintain their original orientation during aggregation-based annealing.

Monte Carlo simulations of the A7 constrained sequence resulted in a 21% decrease in the standard deviation of backbone dihedral angles upon transfer of the peptide from isolation into the capsid environment, demonstrating the rigidity imposed on the fusion peptide (*36*). We believe that the ordering of the nucleated particles with regard to preferred crystallographic orientation along the length of the virus was a result of the stability of the peptide fusion and the symmetry of the virus coat. This nanocrystal ordering promoted the single-crystal nature of the annealed nanowires by satisfying the orientation requirements of the aggregation-based crystal growth mechanism (*15*). Although particles exhibiting orientations that were not coherent with that of the majority were to be expected, these minority nanocrystals should rotate to adopt the preferred crystallographic orientation and merge with the majority during annealing to minimize both the interfacial and grain-boundary energies (*31*, *37*, *38*).

The exploitation of the self-assembly motifs employed by the M13 bacteriophage to produce a biological scaffold provides a means of generating a complex, highly ordered, and economical template for the general synthesis of single-crystal nanowires. By introducing programmable genetic control over the composition, phase, and assembly of nanoparticles, a generic template for the universal synthesis of a variety of materials can be realized. Further advances in the fabrication of nanoscale materials and devices can be achieved through the modification of the remaining four proteins in the virus to incorporate device-assembly directors. Overall, modification of biological systems by the introduction of substrate-specific peptides presents a means of achieving well-ordered nanomaterials in a cost-effective and scalable manner.

Fig. 3. (**A**) CoPt wires, synthesized by the modified virus template, were soluble in water (right). The reduction of Co and Pt salts without the presence of the virus yielded large precipitates which immediately fell out of solution (left). (**B**) TEM image of the unannealed CoPt nanoparticle-virus system. (Inset) STEM image of the unannealed CoPt wires. Scale bar, 100 nm. (**C**) Low-resolution TEM image of crystalline $L1_0$ CoPt wires (650 × 20 nm). The tendency of the CoPt and FePt wires not to be straight stems from magnetic interactions between wires that are not present in the II-VI systems. (Inset) ED shows the characteristic (110) and (001) $L1_0$ lines and the crystallinity of the system. (**D**) HRTEM of the CoPt wires with the (111) plane perpendicular to the *c* axis of the wire. (Inset) ED of an annealed CoPt wire reveals the superlattice structure unique to the $L1_0$ phase. (**E**) TEM imaging of the unannealed FePt wires. (**F**) TEM of the annealed FePt wires. (Inset) ED pattern confirming the $L1_0$ nature of the FePt wires and showing the crystalline nature of the material.

References and Notes
1. R. de Picciotto, H. L. Stormer, L. N. Pfeiffer, K. W. Baldwin, K. W. West, *Nature* **411,** 51 (2001).
2. Y. Wang, L. Zhang, C. Liang, G. Wang, X. Peng, *Chem. Phys. Lett.* **357,** 314 (2002).
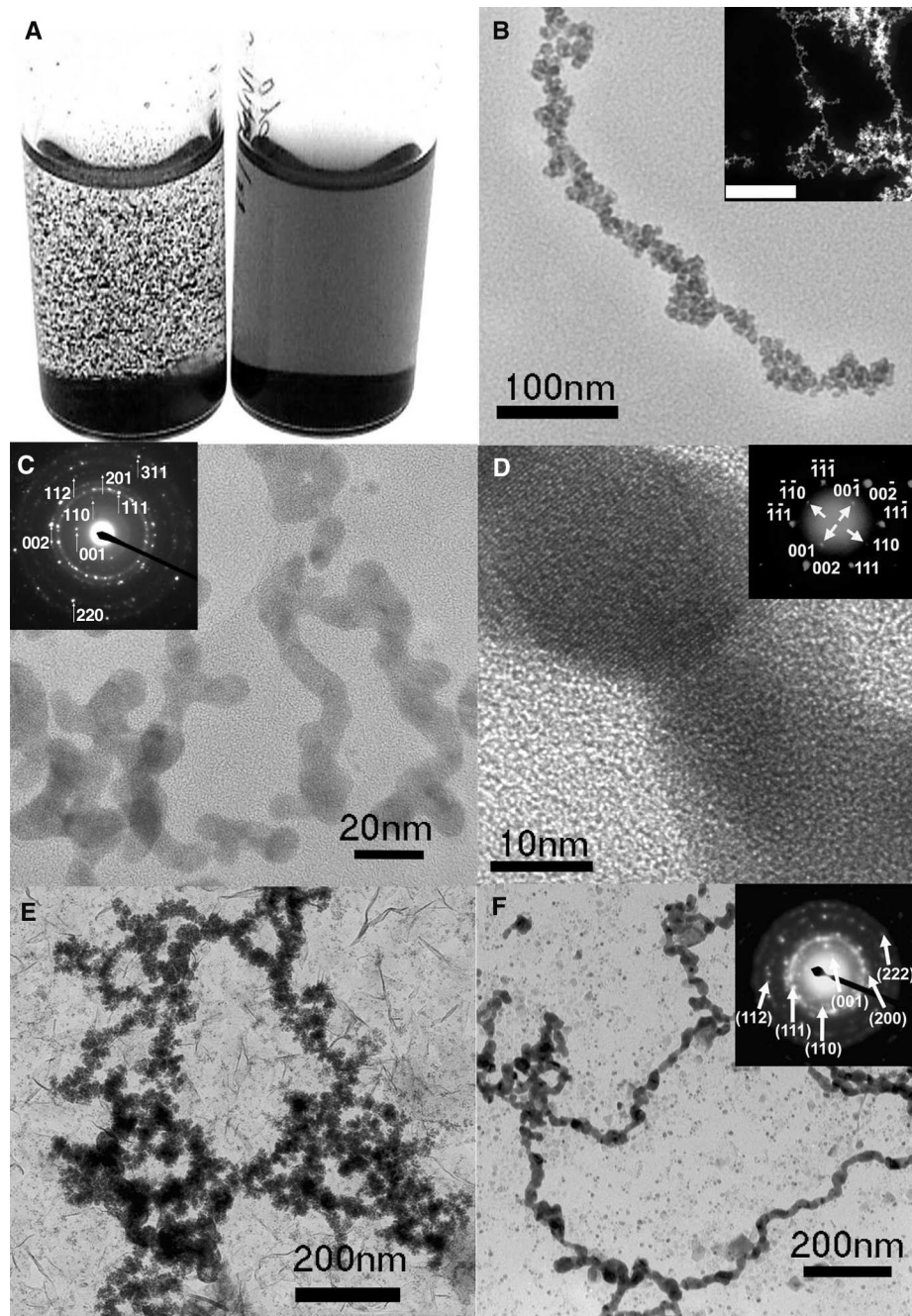
3. Y. Huang *et al.*, *Science* **294**, 1313 (2001).
4. A. M. Morales, C. M. Lieber, *Science* **279**, 208 (1998).
5. L. Manna, E. C. Scher, A. P. Alivisatos, *J. Am. Chem. Soc.* **122**, 12700 (2000).
6. Y. Xia *et al.*, *Adv. Mater.* **15**, 353 (2003).
7. J. N. Cha, G. D. Stucky, D. E. Morse, T. J. Deming, *Nature* **403**, 289 (2000).
8. J. D. Hartgerink, E. Beniash, S. I. Stupp, *Science* **294**, 1684 (2001).
9. T. Douglas, M. Young, *Nature* **393**, 152 (1998).
10. E. Dujardin *et al.*, *Nano Lett.* **3**, 413 (2003).
11. S.-W. Lee, C. Mao, C. E. Flynn, A. M. Belcher, *Science* **296**, 892 (2002).
12. M. Reches, E. Gazit, *Science* **300**, 625 (2003).
13. S. R. Whaley, D. S. English, E. L. Hu, P. F. Barbara, A. M. Belcher, *Nature* **405**, 665 (2000).
14. C. Mao *et al.*, *Proc. Natl. Acad. Sci. U.S.A.* **100**, 6946 (2003).
15. J. F. Banfield, S. A. Welch, H. Zhang, T. T. Ebert, R. L. Penn, *Science* **289**, 751 (2000).
16. A. P. Alivisatos, *Science* **289**, 736 (2000).
17. C. Flynn, *et al.*, *J. Mater. Chem.* **13**, 2414 (2003).
18. B. D. Reiss *et al.*, in preparation.
19. Single-letter abbreviations for the amino acid residues are as follows: A, Ala; C, Cys; D, Asp; E, Glu; F, Phe; G, Gly; H, His; I, Ile; K, Lys; L, Leu; M, Met; N, Asn; P, Pro; Q, Gln; R, Arg; S, Ser; T, Thr; V, Val; W, Trp; and Y, Tyr.
20. C. F. Barbas III *et al.*, *Phage Display, A Laboratory Manual* (Cold Spring Harbor Laboratory Press, Cold Spring Harbor, NY, 2001).
21. C. Gao *et al.*, *Proc. Natl. Acad. Sci. U.S.A.* **96**, 6025 (1999).
22. P. Malik, R. N. Perham, *Nucleic Acids Res.* **25**, 915 (1997).
23. K. Nam *et al.*, *Nano Lett.*, in press; published online 16 December 2003 (10.1021/nl0347536).

24. W. D. Luedtke, U. Landman, *J. Phys. Chem.* **100**, 13323 (1996).
25. Annealing of the ZnS mineralized viruses for 3 hours on aminosilinized SiO_2 wafers at 400° to 500°C, depending on particle size distribution, was followed by sonication in 1:1 water and ethanol. The suspension of annealed wires was drop coated onto TEM grids for visualization. Increasing the wetability of the substrates was necessary for the alignment of the virus assemblies.
26. Thermal gravimetric analysis was performed on the Perkin Elmer 200 thermogravimetric/differential thermal analysis, with flow gases consisting of air, argon, and forming gas (5% H_2). Samples were prepared by centrifugation of the virus-particle suspension into 1-mg pellets and allowed to dry.
27. TEM samples were analyzed with the JEOL 2010 and 2010–Field Emission Gun (FEG) microscopes. HAADF analysis of the ZnS and CdS samples was performed on the JEOL 2010-FEG. Gantan Digital Micrograph is used to subtract the background of the HRTEM lattice images. Thermal analysis of the CoPt system was performed in situ on the JEOL 200CX microscope operated at 200 kV, with a Gatan heat stage.
28. S. B. Qadri *et al.*, *Phys. Rev. B* **60**, 9191 (1999).
29. X. Duan, C. M. Lieber, *Adv. Mater.* **12**, 298 (2000).
30. C. Ye, G. Meng, Y. Wang, Z. Jiang, L. Zhang, *J. Phys. Chem. B* **106**, 10338 (2002).
31. R. L. Penn, J. F. Banfield, *Geochim. Cosmochim. Acta* **63**, 1549 (1999).
32. S. Sun, C. B. Murray, D. Weller, L. Folks, A. Moser, *Science* **287**, 1989 (2000).
33. Y. H. Huang, H. Okumura, G. C. Hadjipanayis, D. Weller, *J. Appl. Phys.* **91**, 6869 (2002).
34. CoPt wires were synthesized by the interaction of 1 ml of CoPt-specific viruses (10^{12} phage/ml) with 0.5 mM $CoCl_2$ and 0.5 mM H_2PtCl_6 in a 1:1 ratio.

In the case of FePt, 1 ml of phage (10^{12} phage/ml) was mixed with 0.01 mM $FeCl_2$ and 0.01 mM H_2PtCl_6. These mixtures were vortexed for 10 min to ensure mixing, and 0.1 M $NaBH_4$ was added to reduce the metals forming the desired nanoparticles. The CoPt and FePt systems were applied directly to SiO TEM grids and annealed under forming gas (5% H_2) to prevent the onset of oxidation for 3 hours at 350°C.
35. K. Barmak *et al.*, *Appl. Phys. Lett.* **80**, 4268 (2002).
36. The virus assembly was reconstructed from the gP8 protein structure obtained from the Protein Data Bank (PDB) (number 1ifj) by application of the appropriate translation vectors. A random number generator was used to realistically incorporate peptide inserts in the gP8 assembly at a given incorporation percentage. The peptide inserts were modeled in the capsid environment with Monte Carlo software MCPRO (*39*) with solvent effects accounted for by the Poisson-Boltzmann toolkit ZAP (*40*).
37. H. Zhu, R. S. Averback, *Philos. Mag. Lett.* **73**, 27 (1996).
38. M. Yeadon, M. Ghaly, J. C. Yang, R. S. Averback, J. M. Gibson, *Appl. Phys. Lett.* **73**, 3208 (1998).
39. MCPRO, Version 1.68; W. L. Jorgensen, Yale University.
40. OpenEye Scientific Software, Cambridge, MA.
41. We thank C. Flynn for valuable discussion. We acknowledge the use of core microscope facilities in the Texas Materials Institute at UT and the Center for Materials Science and Engineering at MIT. Supported by NSF through the Nanotechnology and Interdisciplinary Research Initiative, the Army Research Office, and the Air Force Scientific Research Office.

Boron Nitride Nanomesh

Martina Corso, Willi Auwärter, Matthias Muntwiler, Anna Tamai, Thomas Greber, Jürg Osterwalder*

A highly regular mesh of hexagonal boron nitride with a 3-nanometer periodicity and a 2-nanometer hole size was formed by self-assembly on a Rh(111) single crystalline surface. Two layers of mesh cover the surface uniformly after high-temperature exposure of the clean rhodium surface to borazine $(HBNH)_3$. The two layers are offset in such a way as to expose a minimum metal surface area. Hole formation is likely driven by the lattice mismatch of the film and the rhodium substrate. This regular nanostructure is thermally very stable and can serve as a template to organize molecules, as is exemplified by the decoration of the mesh by C_{60} molecules.

Pairs of boron and nitrogen atoms are isoelectronic to pairs of carbon atoms. Thus, boron nitrides show a structural variety similar to that of carbon solids, including graphitic hexagonal boron nitride (*h*-BN) and diamond-like cubic boron nitride (*c*-BN) (*1*), onion-like fullerenes (*2*), and multi- and single-wall nanotubes (*3*, *4*). Some carbon allotropes, such as C_{60}, are difficult to form as BN analogs, because the formation of B-B or N-N bonds is disfavored, and this property excludes pentagon

formation. We report on a form of BN solid that so far has no analog in carbon allotropes. A highly regular metal-supported BN mesh of nanometer dimensions can be grown by high-temperature chemical vapor deposition on Rh(111). The hexagonal mesh has its basis in the planar, *h*-BN–type bonding and consists of two atomic layers.

Weakly physisorbed layers of *h*-BN on metal surfaces have been studied for about a decade (*5*). Well-ordered films can be grown by thermal decomposition of borazine $(HBNH)_3$ on transition metal surfaces (*6*). In all cases studied so far, the film growth was self-limiting at one monolayer (ML); beyond that, the sticking coefficient of the precursor molecule becomes exceed-

ingly small. Most of the work has been concentrated on the lattice-matched system of *h*-BN on Ni(111), where large terraces of one-ML *h*-BN are formed (*7*). The films are insulating in the sense that the B and N electronic states do not contribute to the Fermi sea of the Ni surface (*8*, *9*). Within this ML, the structure is the expected graphitic sheet, yet with a weak corrugation. The N atoms are located on top of the outermost Ni atoms, and the B atoms occupy face-centered cubic adsorption sites of the Ni(111) surface (*10*, *11*). Depending on the preparation conditions, a second coexisting structure can be found in which the B atoms are placed in hexagonal close-packed adsorption sites. Wherever domains of these different structures coalesce, straight defect lines are observed in scanning tunneling microscopy (STM) images (*12*). Although all these studies illustrated the model character of this weakly physisorbed metal-insulator interface, they did not raise expectations for these systems to exhibit self-organization into complex structures on a nano- to mesoscopic-length scale. Here, it is shown that such self-organization within the *h*-BN layer takes place when deposited on Rh(111), where the lattice mismatch of 6.7% produces a high tensile stress.

The preparation procedure consists of exposing the atomically clean Rh(111) surface, which is kept at a temperature of 1070

Physik-Institut, Universität Zürich, Winterthurerstrasse 190, CH-8057 Zürich, Switzerland.

*To whom correspondence should be addressed. E-mail: osterwal@physik.unizh.ch